Journal of
Synchrotron Radiation

ISSN 0909-0495

Received 8 June 2004
Accepted 17 December 2004

X-ray synchrotron studies of ultrafast crystalline dynamics

Matthew F. DeCamp,[a,b] David A. Reis,[b]* David M. Fritz,[b] Philip H. Bucksbaum,[b] Eric M. Dufresne[b,c] and Roy Clarke[b]

[a]Chemistry Department, Massachusetts Institute of Technology, Cambridge, MA, USA, [b]FOCUS Center and Department of Physics, University of Michigan, Ann Arbor, MI, USA, and [c]Advanced Photon Source, Argonne National Laboratory, Argonne, IL, USA. E-mail: dreis@umich.edu

Ultrafast X-ray experiments at synchrotron sources hold tremendous promise for measuring the atomistic dynamics of materials under a wide variety of transient conditions. In particular, the marriage of synchrotron radiation and ultrafast laser technology is opening up a new frontier of materials research. Structural changes initiated by femtosecond laser pulses can be tracked in real time using time-resolved X-ray diffraction on picosecond time scales or shorter. Here, research at the Advanced Photon Source is described, illustrating the opportunities for ultrafast diffraction with some recent work on the generation of impulsive strain, coherent phonon generation and supersonic diffusion of electron–hole plasmas. The flexibility of time-resolved Bragg and Laue diffraction geometries are both utilized to illuminate the strain generation and evolution process. Time-resolved X-ray science will become increasingly important with the construction of linac-based ultrafast X-ray sources.

Keywords: X-ray diffraction; ultrafast; phonon.

1. Introduction

'Picosecond ultrasonics' is a new field whereby the generation/detection of ultrafast acoustic pulses can be used to study the physical properties of thin films and semiconductors. Precise knowledge of the spatial and temporal dynamics of these laser-generated pulses is required to accurately model the system in question. In crystalline systems, transient coherent lattice dynamics (*i.e.* strain and phonon propagation) are typically studied using time-resolved optical scattering techniques (Thomsen *et al.*, 1984, 1986; Cho *et al.*, 1990; Zeiger *et al.*, 1992; Hunsche *et al.*, 1995; Garrett *et al.*, 1996; Merlin, 1997; Hase *et al.*, 1996, 1998; DeCamp, Reis, Bucksbaum & Merlin, 2001; Bartels *et al.*, 1998; Mizoguchi *et al.*, 1999). Thomsen *et al.* (1986) present a model describing how strain is generated in ultrafast laser-heated solids. Time-resolved optical scattering experiments have demonstrated the general validity of this model (Thomsen *et al.*, 1984, 1986; Hao & Maris, 2000, 2001*a*,*b*) but only provide indirect structural information. The atomic positions cannot be measured directly since the wavelength of optical radiation is orders of magnitude larger than the atomic spacing in a crystal.

X-ray scattering can provide precise information about atomic positions. X-ray scattering can directly measure atomic motion if the motion is slow compared with the natural time scale of X-ray diffraction (X-ray extinction depth divided by the speed of light, $\sim$1 fs). Recent technological advances in femtosecond laser-based X-ray sources and third-generation synchrotron sources have made studies in ultrafast time-resolved diffraction possible (Rousse, Rischel & Gauther, 2001). The high spatial resolution of X-ray scattering, coupled with ultrafast techniques, provides unprecedented insights about solid-state dynamics and can directly test models of coherent strain generation.

Experiments performed with low-frequency ($<$1 GHz) coherent acoustic waves demonstrated the sensitivity of X-ray diffraction to acoustic excitation (Hauer & Burns, 1975; Entin *et al.*, 1978; Zolotoyabko *et al.*, 1993, 2002; Liss *et al.*, 1997). The first sub-nanosecond X-ray diffraction experiments used laser-based X-ray sources to study the propagation dynamics of laser-generated acoustic shockwaves (Wark *et al.*, 1987, 1989; Wark, 1996). The amount of lattice distortion imparted by the shockwave was determined by solving the X-ray wave equation at different times and comparing the calculation with the observed diffraction patterns. These groundbreaking experiments demonstrated the ability of time-resolved X-ray diffraction to detect and measure strong acoustic disturbances in crystals.

Several studies of ultrafast solid-state dynamics using time-resolved X-ray diffraction have utilized laser-based X-ray sources (Chen *et al.*, 1996; Helliwell & Rentzepis, 1997; Rischel *et al.*, 1997; Rose-Petruck *et al.*, 1999; Siders *et al.*, 1999; Cavalleri *et al.*, 2000, 2001; Rousse, Rischel, Fourmaux *et al.*, 2001; Techert *et al.*, 2001; Kishimura *et al.*, 2002; Sokolowski-Tinten *et al.*, 2003). While the time-resolution of laser-based X-ray sources can be sub-picosecond, the

spatial and spectral characteristics of the X-rays from laser-based sources limits their utility.

In contrast, third-generation synchrotron sources offer extremely bright collimated X-ray beams (peak spectral brilliance of $\sim 10^8$ photons $(100\,\text{fs})^{-1}$ mrad^{-2} mm^{-2} $(0.1\%$ bandwidth$)^{-1}$ and offer greater tunability than laser-based X-ray sources. The X-ray pulse duration is limited by the electron bunches which generate the radiation. While the electron bunch length is constrained by various technical considerations to tens of picoseconds or longer (Wiedemann, 1993), X-ray streak cameras can extend the range of synchrotron sources for many experiments to ~ 1 ps resolution. Future linac-based X-ray sources will provide femtosecond X-ray pulses (Winick, 1995). The first such source, the Sub-Picosecond Pulse Source (SPPS) (Service, 2002), has recently been commissioned.

1.1. Time-resolved studies at synchrotrons

The early time-resolved X-ray diffraction experiments at synchrotrons studied laser-induced crystalline melting (Larson *et al.*, 1982, 1983; Tischler *et al.*, 1988). The time resolution of these early experiments was not limited by the X-ray pulse, but rather by the availability of intense sources of sub-nanosecond optical lasers. With the development of chirped pulse amplification (CPA) (Strickland & Mourou, 1985), intense sources of sub-picosecond optical pulses have become commercially available making the time resolution of X-ray scattering at synchrotrons limited only by the X-ray pulse width, $\sim$50–100 ps.

Although 50 ps is relatively slow when compared with the sub-picosecond laser pulse, one can still measure coherent dynamics in crystalline systems (Reis *et al.*, 2001; DeCamp, Reis, Bucksbaum, Adams *et al.*, 2001; DeCamp *et al.*, 2003). A number of advances have extended the effective time resolution to ~ 1 ps. Using a two-crystal cross-correlation technique, Larsson *et al.* (1998) measured a ~ 1 ps structural change using 80 ps X-ray pulses. Direct manipulation of the synchrotron electron beam is also a potential source of fast X-rays. Part of the electron bunch may be displaced by an ultrafast laser. The displaced electron slice generates a sub-picosecond X-ray pulse (Schoenlein *et al.*, 1996; Uesaka *et al.*, 2000). Another method of detecting picosecond structural changes in a long X-ray pulse is using an X-ray streak camera. X-ray streak cameras can achieve a resolution of ~ 1 ps (Chang *et al.*, 1996; Larsson *et al.*, 1997; Liu *et al.*, 2003). Lindenberg *et al.* (2000, 2002) used an X-ray streak camera to measure the frequency spectrum and coherence of an impulsively generated acoustic pulse. Here the study of acoustic pulses is expanded to include a full spectrum analysis of the generated acoustic pulse as well as the study of the long-term ($\sim\mu$s) evolution of acoustic pulses in crystals. We also utilize Laue geometry to study bulk strain propagation.

2. Strain generation

Impulsive excitation is the most direct method of generating a coherent pulse. Short-pulse laser absorption in an opaque material can generate a coherent acoustic pulse if the absorption depth is long compared with the product of the pulse duration and the speed of sound (*i.e.* the impulsive limit) (Thomsen *et al.*, 1986; Akhmanov & Gusev, 1992). If the transverse size of the laser is large compared with the laser absorption depth, then we can consider the resultant strain as uniaxial and planar. This technique has opened a new field of spectroscopy referred to as 'picosecond ultrasonics'. The temporal and spatial profile of the acoustic pulse can reveal critical properties of semiconductors and thin films. The two strain generation mechanisms that have been discussed in the literature are thermo-elasticity and ultrafast carrier diffusion.

2.1. Thermo-elastic model

Thomsen *et al.* (1986) presented a simple thermo-elastic model of strain, which describes the generation and propagation of a laser-induced coherent strain pulse (hereafter referred to as the Thomsen model). In optically opaque crystals an ultrafast laser pulse can be absorbed, depositing a significant amount of energy near the crystal surface. If the electron–phonon relaxation time is extremely fast, this absorption will generate a thermal gradient almost instantaneously. If the illuminated area is large compared with the square of the optical absorption depth, η, the temperature gradient will be quasi-uniaxial in the normal direction (z).

For stress along z, the only non-zero component of the strain tensor is $\eta_{33} = \partial u_3/\partial z$. The thermo-elastic equation of motion is then

$$\rho \frac{\partial^2 u_3}{\partial t^2} = \frac{\partial \sigma_{33}}{\partial z}, \tag{1}$$

where ρ is the density of the material and σ_{33} is the component of the stress tensor in the $\hat{z}$ direction given by

$$\sigma_{33} = v^2 \rho \eta_{33} - 3B\beta\Delta T(z). \tag{2}$$

Here v is the longitudinal sound velocity, B is the bulk modulus and β is the thermal expansion coefficient. The harmonic response of the material is represented by the first term. Assuming that the initial strain is zero and that the stress at the crystal surface is zero, equation (1) can be solved analytically (Thomsen *et al.*, 1986),

$$\eta_{33}(z,t) = (1-R)\frac{F\beta}{\eta C_v}\frac{v^2\rho}{3B}\left\{\exp(-z/\eta)\left[1-\tfrac{1}{2}\exp(-vt/\eta)\right] - \tfrac{1}{2}\exp(-|z-vt|/\eta)\,\text{sgn}\,(z-vt)\right\}, \tag{3}$$

where R is the surface reflectivity, F is the incident optical fluence and C_v is the specific heat per unit volume. Equation (3) represents a lattice strain with two separate components: a static thermal layer and a coherent acoustic pulse. This partitioning of the lattice potential energy is evident in plots of the strain as a function of crystal depth and time (see Fig. 1).

The Thomsen solution uses some physical approximations that can break down on ultrafast time scales. For example, the discontinuity in the center of the acoustic pulse is due to the assumption of instantaneous generation of thermal stress. Time-resolved X-ray diffraction experiments can test these

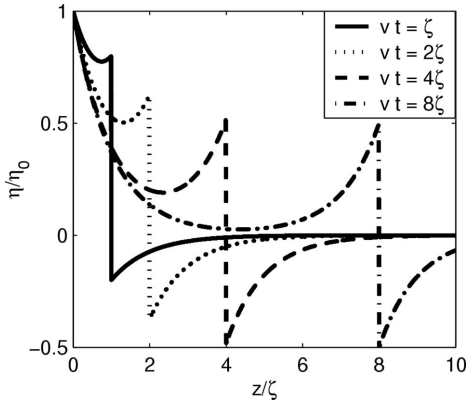

Figure 1
Calculated strain profiles at four different time delays using the Thomsen model.

approximations. A finite electron–phonon coupling time will smooth this discontinuity. It has been measured to be ∼10 ps in many semiconductors (Rose-Petruck *et al.*, 1999; Chin *et al.*, 1999; Lindenberg *et al.*, 2000).

In the Thomsen model, the acoustic pulse shape does not distort with propagation. This assumption is valid only if the acoustic frequencies are relatively small such that $\omega = vk$, where v is the sound speed. In general, the acoustic pulse broadens due to group velocity dispersion by an amount

$$\frac{x\gamma}{c(\Delta z)^2} \tag{4}$$

where Δz is the initial spatial extent of the acoustic pulse, which in the Thomsen model is $\sim 2\eta$. Dispersion becomes significant when the acoustic pulse travels at least a distance z such that

$$x = c(\Delta z)^3/\gamma. \tag{5}$$

For ultrafast acoustic pulses generated by impulsive laser excitation of Ge [$\gamma \simeq 0.85 \times 10^{-11}$ cm^3 s^{-1} (Hao & Maris, 2000)] the acoustic dispersion only becomes important after many meters so we may safely neglect it.

2.2. Ultrafast carrier diffusion

During intense laser excitation, a large dense electron–hole plasma is generated at a crystal surface (Young & van Driel, 1982). This dense plasma can diffuse into the material at supersonic velocities, creating stress deep within the material.

The initial electron–hole plasma density depends on the optical penetration depth. In the simplest case, the density decreases exponentially away from the surface,

$$n(z, t = 0) = n_0 \exp(-z/\eta)/\eta, \tag{6}$$

where n_0 is the number of photons per unit area absorbed. We assume that the time-dependence of this plasma is governed by carrier diffusion and Auger recombination,

$$\frac{\mathrm{d}n}{\mathrm{d}t} = D_p \frac{\mathrm{d}^2 n}{\mathrm{d}z^2} - An^3, \tag{7}$$

where D_p is the carrier diffusion constant and A is the Auger recombination rate.

In the limit of fast carrier relaxation, the temperature profile is proportional to n,

$$T(z, t = 0) = n(z, t = 0)\frac{E_p - E_g}{C_v}, \tag{8}$$

where E_p and E_g are the photon energy and the electronic band gap, respectively, and C_v is the crystalline heat capacity. The temperature evolution is governed by thermal and carrier diffusion, and Auger recombination,

$$\frac{\mathrm{d}T}{\mathrm{d}t} = D_t \frac{\mathrm{d}^2 T}{\mathrm{d}z^2} + An^3 \frac{E_g}{C_v}, \tag{9}$$

where D_t is the thermal diffusion constant.

We assume that the surface strain profile is driven by the temperature gradient and the plasma density,

$$\eta_e(z, t) = \alpha_t T(z, t) + \alpha_p n(z, t), \tag{10}$$

where η_e is the surface strain and α_t and α_p are the coupling constants for the temperature and plasma components, respectively. As the plasma diffusion can be much faster than the sound velocity, the initial strain front can travel into the crystal bulk at supersonic speeds producing a spatially broadened acoustic pulse. In the case of Ge, the spatial broadening of the acoustic pulse can be more than a factor of five when compared with the thermo-elastic model (Cavalleri *et al.*, 2000, 2001; DeCamp *et al.*, 2003).

3. Calculating time-resolved X-ray diffraction patterns

The strain changes the phase-matching condition for X-ray diffraction: $\mathbf{k}_0 + \mathbf{G} = \mathbf{k}$, where $\mathbf{k}_0$ is the incident wavevector, $\mathbf{G}$ is a reciprocal lattice vector and $\mathbf{k}$ is the diffracted wavevector. For a phonon wavevector of $\mathbf{q}$, the diffraction peak develops sidebands corresponding to the modified phase-matching condition $\mathbf{k}_0 + \mathbf{G} \pm \mathbf{q} = \mathbf{k}_{\pm q}$. For a phonon wavevector parallel to the reciprocal lattice vector, the sideband is centered at an offset angle $\Delta\theta \simeq q/G \tan\theta_\mathrm{B}$ from the main X-ray diffraction peak (where θ_B is the Bragg angle). In addition, the scattered X-rays at a given offset will experience a small frequency shift $\omega = \omega_0 \pm \Omega$ owing to the absorption or emission of a phonon of frequency $\Omega = qv_s$ (stimulated Brillouin scattering), where v_s is the speed of sound. The sideband at a particular q will oscillate at the corresponding frequency Ω owing to the interference of X-rays of frequency ω_0 and $\omega_0 \pm \Omega$.

Simulations of the X-ray reflectivity for thick crystals (when X-ray absorption is non-negligible) must use the dynamical theory of X-ray diffraction (Zachariasen, 1945; Batterman & Cole, 1964; Warren, 1990). In dynamical diffraction, the X-ray wavefield is calculated by solving Maxwell's equations in a material with a periodic and complex dielectric constant.

3.1. Dynamical diffraction theory in the presence of strain

In a perfect unstrained crystal, two linearly independent solutions to Maxwell's equations satisfy the diffraction

condition. These two solutions (α and β) can be graphically represented as a hyperboloid in reciprocal space, *i.e.* the dispersion surface. These solutions are transverse X-ray standing waves with the α (β) solution having its nodes (antinodes) on the diffracting lattice planes. Since the X-ray absorption is dominated by the photoelectric absorption, the α solution can propagate through the crystal with little or no attenuation, whereas the β wave is attenuated at twice the average X-ray absorption depth. In the Laue geometry, the α solution is referred to as anomalous transmission of X-rays or the Borrmann effect. In the Bragg geometry, a single beam emerges from the crystal whereas, in the Laue case, emerging from the crystal are two diffracted beams: one in the direction of the input beam (forward-diffracted or '0' beam) and the other in the direction determined by the vector sum $\mathbf{k}_H = \mathbf{k}_0 + \mathbf{G}_H$ (deflected-diffracted or 'H' beam). Here $\mathbf{k}_0$ ($\mathbf{k}_H$) corresponds to the wavevector of the forward-diffracted (deflected-diffracted) beam and $\mathbf{G}_H$ is the reciprocal lattice vector corresponding to the diffracting planes. These beams are linear combinations of the two internal solutions, α and β. Their intensities are given by

$$I_0 = |a\mathbf{E}_\alpha \exp(i\mathbf{k}_\alpha \cdot \mathbf{z}) + b\mathbf{E}_\beta \exp(i\mathbf{k}_\beta \cdot \mathbf{z})|^2 \propto |\mathbf{E}_0|^2, \quad (11)$$

$$I_H = |c\mathbf{E}_\alpha \exp(i\mathbf{k}_\alpha \cdot \mathbf{z}) - d\mathbf{E}_\beta \exp(i\mathbf{k}_\beta \cdot \mathbf{z})|^2 \propto |\mathbf{E}_H|^2, \quad (12)$$

where I_0 (I_H) is the diffracted intensity of the forward (deflected) beam, $\mathbf{E}_{\alpha,\beta}$ is the field amplitude inside the crystal, $\mathbf{k}_\alpha$ and $\mathbf{k}_\beta$ are the complex wavevector of the α and β solutions (including absorption), respectively, and a, b, c, d are determined by the crystal orientation. The two modes α and β have different phase velocities and oscillate in and out of phase with each other as they propagate through the crystal. The wavelength of the interference, $\Lambda = |\mathbf{k}_\alpha - \mathbf{k}_\beta|^{-1}$, is known as the Pendellösung length which is typically a few to tens of micrometers.

In large crystals, the Pendellösung effect has been used to image static crystalline defects. Defects located well beyond the β wave absorption depth cause a repopulation of the β solution at the expense of the α wave. The location and size of the defect can be determined by measuring the change in the intensity of the diffracted beams (Taupin, 1964; Authier *et al.*, 1996).

To incorporate strain, we consider the case where the X-rays are near phase matched for diffraction from a single set of planes, $\mathbf{G}_H$. Using an eikonal approximation for the field amplitudes in the presence of static strain as given by Takagi (1962, 1969) and independently by Taupin (1964), the electric displacement amplitudes are given by two coupled differential equations, valid for either the Bragg or Laue geometry,

$$i(\lambda/\pi)\boldsymbol{\beta}_0 \cdot \nabla D_0(r) = \psi_0 D_0(r) + \psi_H D_H(r), \quad (13)$$

$$i(\lambda/\pi)\boldsymbol{\beta}_H \cdot \nabla D_H(r) = \psi_0 D_H(r) + \psi_H D_0(r) - \gamma D_H(r), \quad (14)$$

where λ is the X-ray wavelength in a vacuum, D_0 and D_H are the electric displacement fields inside the crystal, γ [$= -2(\theta - \theta_B)\sin 2\theta_B$] is the offset from the Bragg condition, ψ_0 and ψ_H are the 0 and H Fourier coefficients of the crystal electric susceptibility, respectively, and $\beta_{0,}$ and β_H are the wavevectors inside the crystal. The crystalline strain is taken into account by modifying γ to represent a crystal with a slightly modified lattice spacing. In the Bragg (reflection) geometry, equations (13) and (14) can be combined to form a single first-order differential equation in the ratio of the field amplitudes, $x = D_H/D_0$ (Wie *et al.*, 1986). As the index of refraction is almost unity, $|x|^2$ is effectively the X-ray reflectivity.

The Takagi–Taupin approximation requires that the spatial strain gradient varies slowly compared with the spacing of the diffracting planes (*i.e.* $|q| \ll |G|$), a condition that is well satisfied for laser-generated strains. In addition, we assume that the time derivatives of the field amplitudes are negligible corresponding to the limits that the phonon frequency $\Omega \rightarrow 0$ (*i.e.* $v_s \ll c$) and that the X-ray propagation time through the crystal is small compared with the X-ray pulse duration (Wark & He, 1994; Tomov *et al.*, 1998). Solving these equations at different time delays between the X-ray probe and the laser pump, the time dependence is reintroduced. The strain propagation is accounted for at each time delay.

4. Experimental set-up

The experiments were performed at the MHATT-CAT sector 7 insertion-device beamline at the Advanced Photon Source (APS) at Argonne National Laboratory. The facility includes an amplified ultrafast laser synchronized to the X-ray source for time-resolved X-ray scattering experiments. Most of the experiments are performed using the laser to repetitively pump the sample of interest, whereas the X-rays are used to probe the structure at a precisely controlled and variable delay. In this manner, one can build up a picture of the dynamics frame by frame. In such pump–probe techniques, the temporal resolution is limited to the probe pulse duration allowing for relatively slow detectors (1–10 ns response time) to be used.

A schematic of the experimental set-up is shown in Fig. 2. The X-rays from the synchrotron correspond to a series of pulses synchronized to the circulating current in the stored electron beam. On average, it takes an electron in the storage ring exactly 1296 cycles of the 352 MHz accelerating RF (buckets) to travel once around the 1.1 km ring. The stored current consists of a number of electron bunches each of $\sim$100 ps (FWHM) duration. Typically, just a few of the 1296 buckets are filled. The standard bunch pattern corresponds to 23 single bunches spaced every 54 buckets ($\sim$150 ns) followed by a 54 bucket gap.

4.1. X-ray optics

The X-rays are produced as the electrons pass through a 2.4 m, 3.3 cm-period permanent-magnet undulator. For time-resolved experiments there are two standard modes of operation: polychromatic ('pink' beam) or monochromatic X-ray production. Pink-beam operations (which could be used for time-resolved X-ray absorption spectroscopy, crystal-

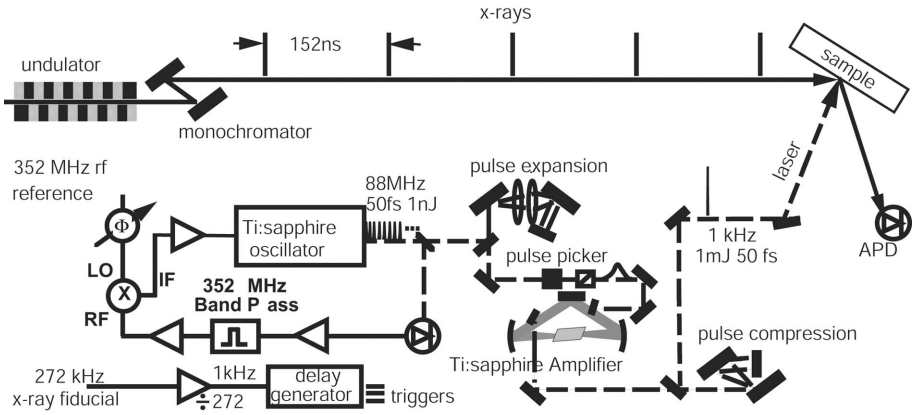

Figure 2
Experimental set-up for pump–probe time-resolved X-ray diffraction.

lography or protein crystallography) provide an average photon current of up to 3×10^{15} photons s^{-1} in a $\sim$2% bandwidth. For the experiments described here, the beamline was configured for monochromatic X-ray production.

The X-rays are monochromated by a cryogenically cooled Si(111) double-crystal monochromator $\sim$30 m from the source. Typical operations are at 10 keV with an average flux of 2×10^{13} photons s^{-1} at 100 mA stored beam within a 1.4 eV bandwidth (Dufresne *et al.*, 2002). The sample is mounted on a four-circle goniometer $\sim$55 m from the source. Before the sample, the X-ray beam cross section is approximately 1 mm^2. Typically slits placed <1 m from the sample are used to both collimate and aperture the beam. For experiments that require higher flux, both compound refractive lenses (Dufresne *et al.*, 2001; Arms *et al.*, 2002) or a dynamically bent Kirkpatrick–Baez mirror pair can be used for small beam applications. Ionization chambers both before and after the sample monitor the average X-ray current along the beamline.

Diffraction conditions of the monochromator do permit a significant amount of third harmonic of the undulator to propagate to the experiment ($\sim$10% of the fundamental). To remove the third harmonic a grazing-incidence tungsten mirror is used 24 m downstream of the monochromator. The reflectivity of the tungsten mirror reduces the third harmonic by a factor of 100 while giving the user the ability to coarsely steer the X-ray beam.

4.2. Laser system

The laser system is based on chirped pulse amplification (Strickland & Mourou, 1985; Backus *et al.*, 1998). The laser system is shown in the experimental set-up in Fig. 2. The front end is a Kerr-lens mode-locked Ti:sapphire oscillator which produces a train of 40 fs (FWHM) near-infrared ($\sim$800 nm) pulses at a repetition rate of 88 MHz. The repetition rate is locked to the fourth sub-harmonic of the APS accelerator cavities such that the pulse train is synchronized with the circulating electron beam and with the X-ray pulses from the undulator. The oscillator pulses are chirped to approximately 20 ps (over the $\sim$30 nm bandwidth) and a single pulse is selected for amplification by a Pockels' cell at $\sim$1 kHz, timed to a single X-ray bunch. The single laser pulse is amplified by approximately 60 dB to $\sim$1.2 mJ in an eight-pass Ti:sapphire amplifier. The chirped pulse may be used for time-resolved experiments that require maximal temporal overlap with the X-ray pulse. For the experiments described here, the amplified pulse was subsequently compressed back to $\sim$40 fs with a maximum pulse energy of $\sim$0.7 mJ.

The laser pulse is directed onto the sample of interest. The optical fluence is controlled by using a waveplate–polarizer pair and a lens. Many experiments operate just below the damage threshold. Active feedback on the oscillator cavity length reduces the timing jitter between the laser and the X-ray pulses to about 10–20 ps (r.m.s.). A recent upgrade has reduced the jitter to $\sim$2 ps r.m.s. A combination of a digital phase shifter in the reference RF and the digital delay of the Pockels' cell trigger controls the timing of the amplified laser with 19 ps precision to any one of the X-ray pulses. Finer delay is possible by optical methods. The time delay of the laser with respect to a single X-ray bunch may be scanned over as much as a -1 to 1 ms range (limited only by the repetition rate of the laser) while maintaining picosecond precision and stability. The 88 MHz repetition rate of the laser oscillator corresponds to every fourth cycle in the storage ring. Therefore, in the recently implemented 324 bunch mode of the APS, experiments could utilize each X-ray bunch with the laser oscillator beam.

4.3. Time-resolved detectors

4.3.1. APD. Ultrafast time-resolved diffraction measurements require X-ray detectors that can differentiate between individual X-ray bunches emitted by the synchrotron. A silicon avalanche photodiode (APD) is used to temporally isolate a single X-ray pulse (Baron, 1997). If the silicon is thick, the quantum efficiency of the APD is close to unity, while the rise time is fast enough to temporally resolve the singlet spacing of the emitted X-ray bunches (3–5 ns, see Fig. 3). The detector is then gated to measure the average intensity of any given X-ray bunch.

4.3.2. Streak camera. X-ray picosecond streak cameras can resolve dynamics that occur within a single X-ray pulse (Chang *et al.*, 1996; Larsson *et al.*, 1997; Liu *et al.*, 2003). The time resolution of the streak camera used in the experiments described here was $\sim$5 ps.

We have recently developed a compact picosecond streak camera based on the design of Chang *et al.* (1996). Secondary photoelectrons emitted from a CsI photocathode follow the X-ray temporal profile and are accelerated and streaked by meander-type (group velocity matched) transverse deflection plates. The high-voltage pulse for the plates is generated using

a photoconductive switch triggered by a small fraction of the amplified laser pulse. The camera is lightweight, such that it can mount directly on the detector arm of the four-circle goniometer, and it operates at the 1 kHz repetition rate of the laser. The resolution of this camera is 2 ps over a dynamic range of 100 ps (see Fig. 4).

5. Time-resolved Bragg diffraction

Time-resolved X-ray Bragg diffraction was used to measure the amplitude and frequency spectra of the impulsively generated phonons in InSb. InSb is an ideal crystal to begin the study of acoustic phonon generation owing to its small optical penetration depth (∼100 nm) and relatively slow sound speed (∼3400 m s^{-1} in the 111 direction). A significant fraction of the incident laser energy is absorbed in the crystal causing an increase in the average surface temperature. At modest laser fluences (∼10 mJ cm^{-2}) the laser does not cause surface melting, though over many laser pulses surface scarring is visible. This scarring did not affect the X-ray diffraction patterns indicating that damage was only on the surface.

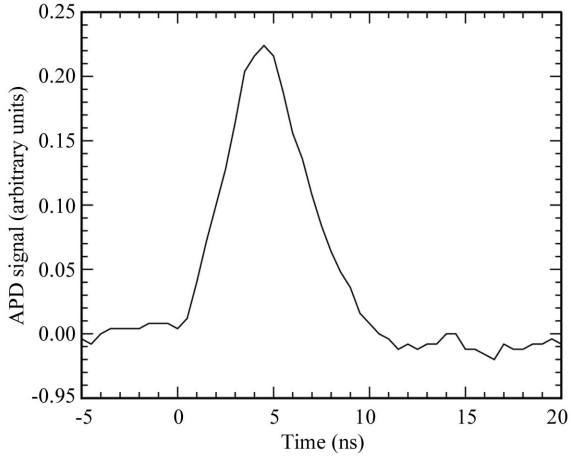

Figure 3
Temporal response of the APD.

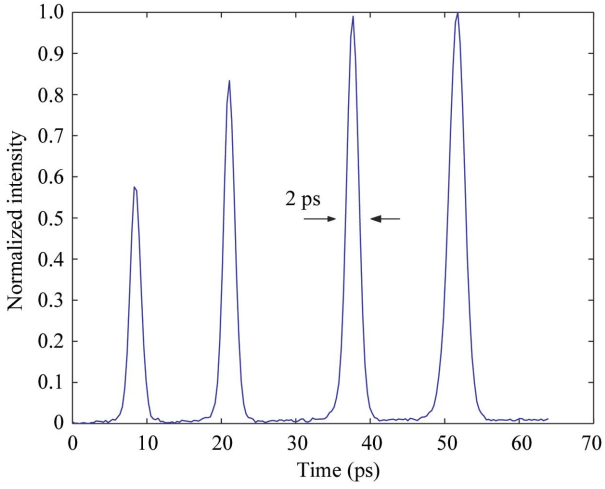

Figure 4
Temporal response of the streak camera.

The rise in temperature owing to repetitive laser exposure causes the average spacing of the crystal lattice to increase, shifting the location of the diffraction peak (Fig. 5). We find the lattice parameter has expanded by ∼0.26 mÅ. Assuming a linear expansion coefficient of 4.7×10^{-6} K^{-1} (Lide, 1996), the temperature increase is ∼15 K.

The strain is significantly larger at the moment following laser excitation. Fig. 6 shows sidebands on either side of the diffraction peak 100 ps after the laser pulse. In the kinematic diffraction limit these could indicate that there are three regions inside the crystal: unstrained, compression (positive sidebands) and rarefaction (negative sidebands). Less than 1 ns after the laser excitation, the shape of the diffraction pattern has almost returned to normal, though the diffraction peak has shifted by ∼3 mdeg indicating that the initial strain has either dissipated or propagated out of the detection region leaving a residual heated layer at the surface. The significant

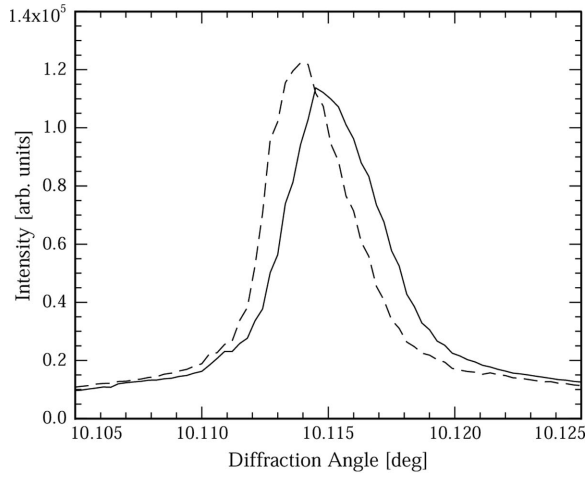

Figure 5
Rocking curve of the laser-heated (dashed) and the unstrained InSb symmetric 111 reflection taken with an ionization chamber.

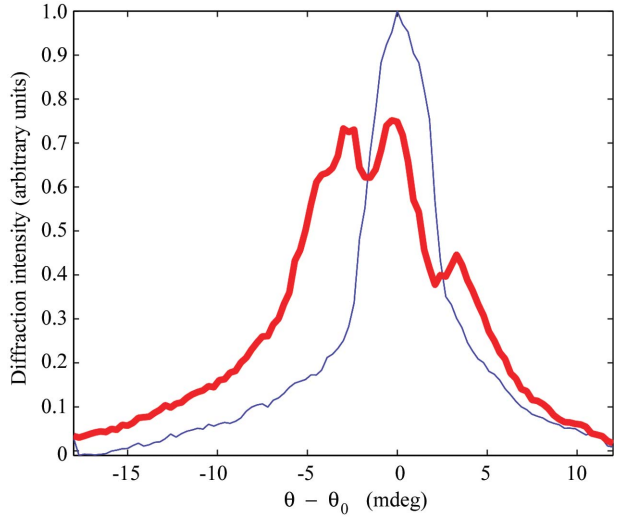

Figure 6
The diffraction patterns of the 111 InSb at time delays of −100 ps (thin line) and 100 ps (thick line).

angular shift indicates that the 'static' thermal layer at the crystal surface has risen at least 60 K.

Individual rocking curves at different time delays reveal a picture of the strain (Fig. 7). At zero time delay, sidebands are apparent on the main Bragg peak. The positive sidebands only remain for ~400 ps whereas the negative sidebands exist for ~500 ps and show time-dependent oscillations. This implies that the compression layer leads the rarefaction layer out of the detection region. At each discrete angle a Fourier transform of the time axis is performed (Fig. 7*b*). The peak position of the Fourier transform changes linearly with diffraction angle. Since the deviation from the Bragg condition is a measurement of phonon momentum, the time-resolved X-ray diffraction is a graphical representation of the acoustic dispersion relation, $\omega = vk$.

Data taken with the symmetric 004 reflection in single-crystal Ge show qualitatively similar features to the InSb data (Fig. 8), including the immediate generation of sidebands on either side of the rocking curve and the existence of a 'static' heated layer. Upon closer inspection there are two distinct differences between the InSb and the Ge cases. The most apparent difference is the global increase in diffraction intensity at positive time delays owing to the intrinsically small X-ray diffraction linewidth of the Ge reflection. The X-ray reflectivity rises when the Ge crystal is distorted owing to the increased width of the rocking curve. The second difference is the lack of time-dependent modulations on either side of the diffraction peak in Ge. This is due to the faster sound speed (~4800 m s^{-1}) and the larger Bragg angle which makes the time-dependent oscillations faster than the X-ray pulse width.

5.1. Comparison: experiment *versus* theory

Dynamical diffraction theory is used to model the diffraction patterns. Quantitative comparisons between the data and the strain generation models presented above are possible. To accurately represent the data, 'real world' constraints (*i.e.* X-ray bandwidth of 1.4 eV and 100 ps pulse width) are included in the calculation (see Fig. 9). If the strain is determined by the Thomsen model, the general structure of the InSb and Ge data are well represented by the simulations. In the case of InSb, the time-dependent oscillations, as well as the lifetime of the sidebands, are correctly predicted. In the case of Ge, the increase in diffraction efficiency (*i.e.* the number of scattered photons at a specific diffraction angle) and the existence of an interference fringe crossing the diffraction peak is correctly predicted.

Although these general features are reproduced, there are distinct differences between the Thomsen strain model and the experiments. In the case of InSb, the calculation does not correctly reproduce the relative amplitudes of the generated sidebands. Changing the relative partitioning of the acoustic pulse and the static strained layer accurately reproduces the data (Reis *et al.*, 2001). The strain in the Ge case also requires significant modification. The compression sideband is visible long after the prediction of the Thomsen model has decayed. It has been suggested that ultrafast carrier diffusion modified the depth where the strain is generated in Ge (Cavalleri *et al.*, 2001). The carrier diffusion initially produced a strain up to 1 μm in depth, five times the optical penetration depth. A diffraction calculation assuming carrier diffusion is shown in Fig. 10. The time scale and magnitudes are well represented by the carrier diffusion model.

5.2. Acoustic pulse evolution

Time-resolved diffraction experiments using strong Bragg reflections are limited to the study of strains within the X-ray extinction depth. For allowed Bragg reflections, this length scale is typically ~1 μm. A quasi-forbidden reflection, however, can probe depths as large as the incoherent X-ray absorption depth, which can be orders of magnitude greater than the X-ray extinction depth of the strong Bragg reflection (Reis *et al.*, 2001). Although this is an attractive solution, the diffraction efficiency of a quasi-forbidden reflection is very small making precise measurements of the strain very difficult. Acoustic reflections can extend the number of detection times inside the crystal by allowing the acoustic strain to re-enter the detection region several times. In this way, strong X-ray Bragg diffraction can then be used to study acoustic pulse evolution over long times.

If the crystal surfaces are highly polished, the impedance mismatch at a crystal/air interface will allow a reflection of an acoustic pulse. At the reflection, the acoustic pulse will experience a π phase shift since the impedance of the air at the crystal surface is approximately ∞ (Woolsey & Wark, 1997; Hao & Maris, 2000), so that at the time of acoustic collision the peak surface strain is double the amplitude of the acoustic pulse.

An acoustic pulse is generated in a 280 μm-thick piece of single-crystal (001) Ge, with both faces polished to optical quality (Fig. 11). At regular intervals (~110 ns) the X-ray diffraction intensity increases dramatically for a short period of time (~3 ns) while a relatively slow time-dependent background decays with a time constant of ~150 ns. The characteristic periodic increase in diffraction efficiency is due to the acoustic pulse re-entering the X-ray detection region after reflecting off the back of the crystal. The slowly decaying background is due to thermal diffusion relaxing the surface strain. The angular dependence of the diffraction revivals can be measured to determine the shape of the acoustic pulse over long periods of time. Fig. 12 shows the time-resolved X-ray diffraction measurement of the first and tenth returns of the acoustic pulse. The first revival corresponds to the acoustic pulse travelling ~550 μm while the tenth revival corresponds to an acoustic pulse travelling ~5.55 mm.

To simulate the data, it is assumed that the acoustic pulse has a spatial extent of 2 μm, consistent with carrier diffusion. It is assumed that during the first revival the static heated layer has decreased in amplitude by a factor of four, while the tenth revival does not have a heated layer. The peak strain was varied so that the simulation would fit the data accurately. The first revival is consistent with a symmetric strain pulse (Fig. 13). The compression sideband increased owing to the

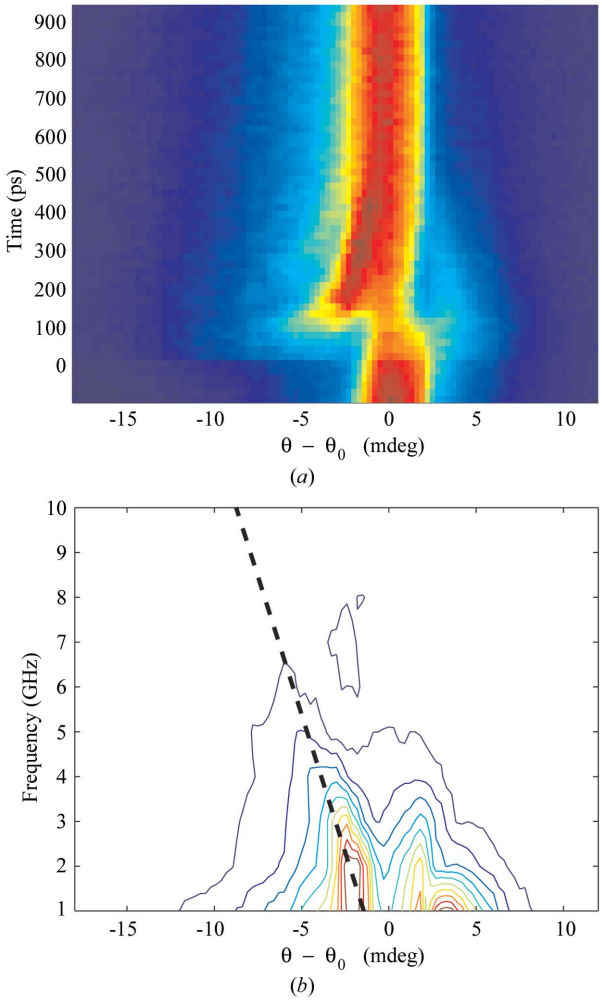

Figure 7
(*a*) Time-resolved Bragg diffraction curves of the symmetric 111 reflection in laser-strained InSb. Adapted from Reis *et al.* (2001). (*b*) Fourier transform of the time-resolved Bragg diffraction. The dashed line is the calculated dispersion relation for the longitudinal sound speed for InSb.

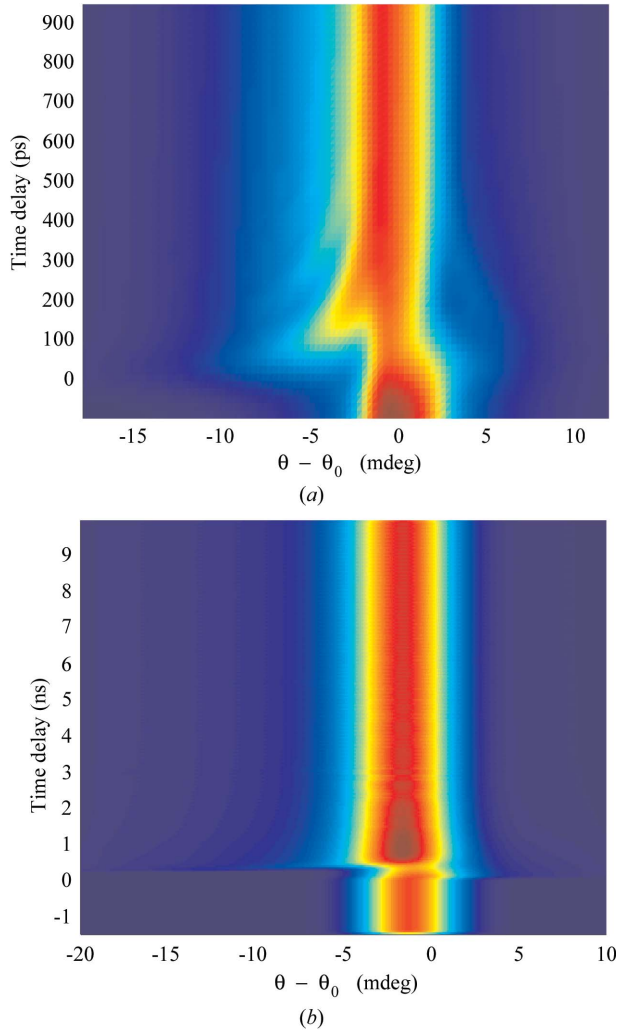

Figure 9
(*a*) Time-resolved Bragg diffraction of InSb using the Thomsen model of strain incorporating 'real world' constraints. Adapted from Reis *et al.* (2001). (*b*) 'Real world' simulation of time-resolved Bragg diffraction using the 400 reflection in Ge.

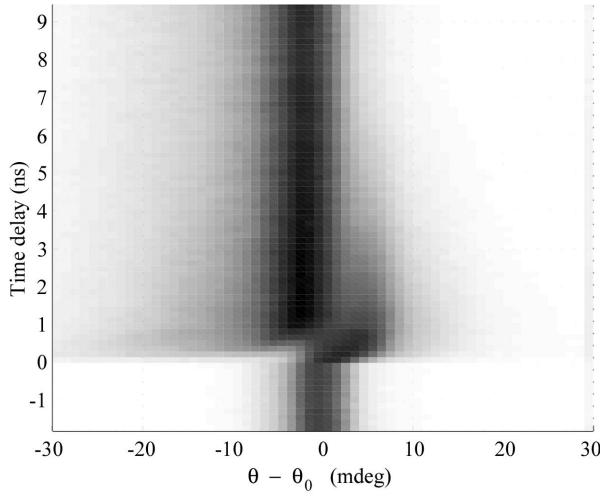

Figure 8
Time-resolved Bragg diffraction curves of the symmetric 400 reflection in laser-strained Ge.

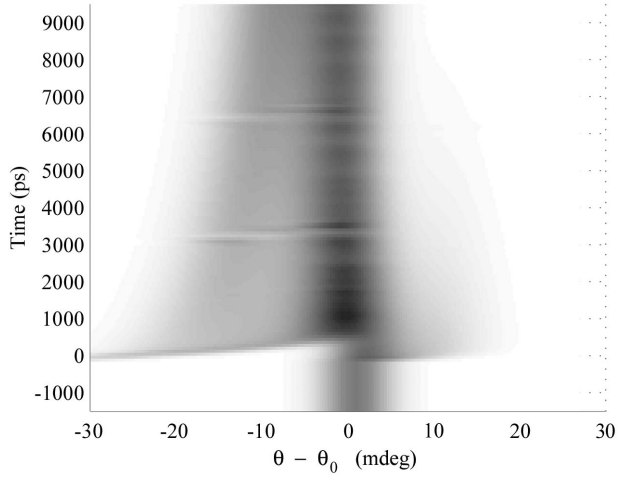

Figure 10
Simulation of the time-resolved strain in Ge assuming the strain was generated by ultrafast carrier diffusion. The beats at ∼3200 ps and ∼6500 ps are due to numerical artifacts.

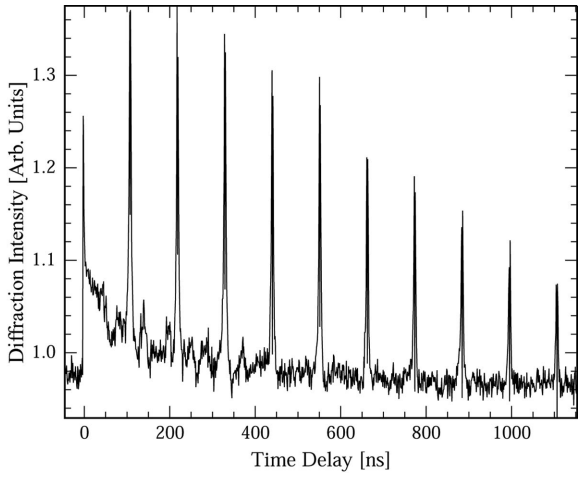

Figure 11
Diffracted X-ray intensity as a function of time delay.

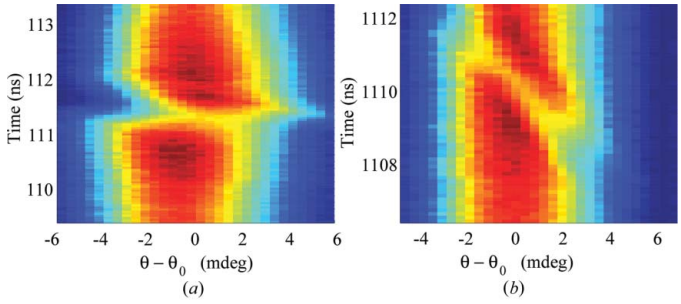

Figure 12
Time-resolved diffraction at an acoustic reflection: (*a*) first revival, (*b*) tenth revival.

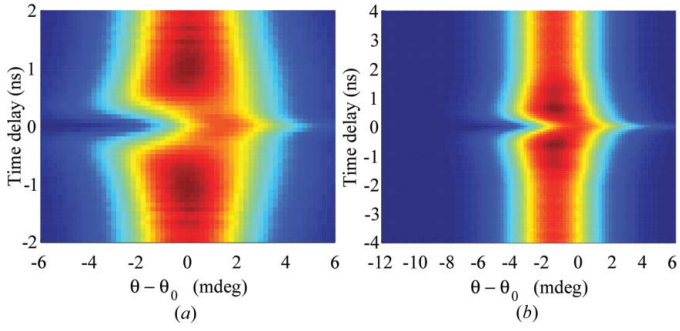

Figure 13
Simulation of an acoustic pulse reflection from a Bragg reflection surface. (*a*) Static heated layer included to represent the first revival; (*b*) static layer not included to represent the tenth revival.

doubling of the strain at the crystal surface, while the rarefaction sideband diminished owing to the self-interference of the acoustic pulse. The interference fringe takes 0.5 ns to cross the entire diffraction peak which is consistent with a 2 μm acoustic pulse. Later reflections, however, do not appear to follow the 2 μm acoustic pulse. The large momentum components have disappeared leaving only the low-frequency components of the acoustic pulse while the interference fringe crosses the entire diffraction peak in about 3 ns, implying that the acoustic pulse has spatially broadened by over 10 μm.

Group velocity dispersion should be negligible here. The cause of the observed dispersion is not yet known, although there are a few possible explanations. First, the crystal faces may not be perfectly polished giving the crystal surface variations of the order of the acoustic wavelength. Owing to wave diffraction effects, the high-frequency components of the acoustic pulse will diffract much faster than the low frequencies leading to an effective spatial broadening. The second possible reason is a non-linear frequency attenuation within the crystal.

6. Time-resolved X-ray transmission

Although X-ray Bragg diffraction is an effective tool for studying time-dependent strains, the small extinction depth of the diffracting X-rays does not allow the continuous monitoring of a propagating strain in thick crystals. The Laue geometry can circumvent this problem since the X-rays will now diffract throughout the bulk of the crystal.

X-ray transmission is typically limited to very thin crystals (<10 μm) or very large X-ray energies (>20 keV). Although thick crystals can be probed with high-energy X-ray photons, the generation and detection of these photons makes time-resolved experiments difficult (APDs and photocathodes are not efficient detectors of >20 keV photons). Nevertheless, coherent acoustic phonons with MHz frequencies have been studied using 30 keV X-rays in the Laue geometry (Liss *et al.*, 1997).

Crystallographers have studied lattice dislocations and crystal defects in crystals that are much deeper than the incoherent absorption depth using X-ray anomalous transmission (Authier *et al.*, 1996). Time-resolved studies using the Borrmann effect have been extremely limited (Le Roux *et al.*, 1975, 1976). This section reports data on novel time-resolved experiments using X-ray anomalous transmission.

Two diffraction geometries are discussed: the symmetric Laue geometry where the reciprocal lattice vector is perpendicular to the crystalline surface normal, and the asymmetric Laue geometry. In the symmetric Laue geometry, the laser-generated strain is perpendicular to the reciprocal lattice vector. This geometry allows the study of transverse strains and/or higher-order phonon coupling to X-ray diffraction. Asymmetric Laue diffraction is more sensitive since the generated strain has a component along the reciprocal lattice vector.

6.1. Time-resolved diffraction in the symmetric Laue geometry

For experiments performed in the symmetric Laue geometry, a (001) Ge single crystal is oriented to diffract 10 keV X-rays from the symmetric 220 diffraction plane. At large laser fluences (>5 mJ cm^{-2}) the generated thermal gradient distorts the crystal causing the X-ray anomalous transmission to be diminished in ∼100 ns (Fig. 14). As the crystal reaches a thermal equilibrium, the strain is relieved and the anomalous transmission recovers. However, if the laser

pulse melts the material (fluences >50 mJ cm^{-2}), repetitive laser heating ($\sim 10^6$ laser shots) permanently strains the crystal through imperfections in the recrystallization process. After several shots, the induced static strain permanently reduces the X-ray transmission.

Borrmann's original experiments demonstrated the loss of X-ray anomalous transmission as a crystal experiences a thermal gradient (Borrmann & Hildebrandt, 1956). It was demonstrated in a thick calcite crystal that a thermal gradient of only 0.2 K cm^{-1} is sufficient to destroy the anomalous transmission. The thermal gradient generates a static stress such that the X-ray waveguide is destroyed, causing complete absorption.

As the laser fluence is reduced, the smaller temperature gradient allows the observation of long-term changes in the X-ray transmission. Fig. 15(*a*) shows the diffracted intensity of the forward and deflected beams as a function of time delay (incident fluence ~ 1 mJ cm^{-2}). Immediately after the absorption of the laser pulse, the intensities of the two diffracted beams begin to oscillate. As the time delay increases, the intensities of the forward and diffracted beams oscillate out of phase with a period of ~ 1.7 ns. The amplitude of oscillations decreases with a decay constant of ~ 10 ns. Time delays greater than 27 ns display a revival of the time-dependent oscillations. The oscillations grow in amplitude with the same time constant and period that was observed at earlier time delays. However, the observed modulations in the diffracted beams now oscillate in phase. At a time delay of ~ 55 ns the amplitude reaches a maximum. This time delay corresponds to the traversal time of the acoustic pulse through the 280 µm-thick crystal. Similar features occur when the acoustic pulse starts at the input face of the crystal (Fig. 15*b*). Here the phase of the two diffracted beams changes. At times close to zero time delay the beams oscillate in phase while at delays of ~ 55 ns the beams oscillate out of phase. Dynamical diffraction theory can explain these features.

The observed period of oscillation equals the ratio of the Pendellösung period to the longitudinal sound speed of Ge.

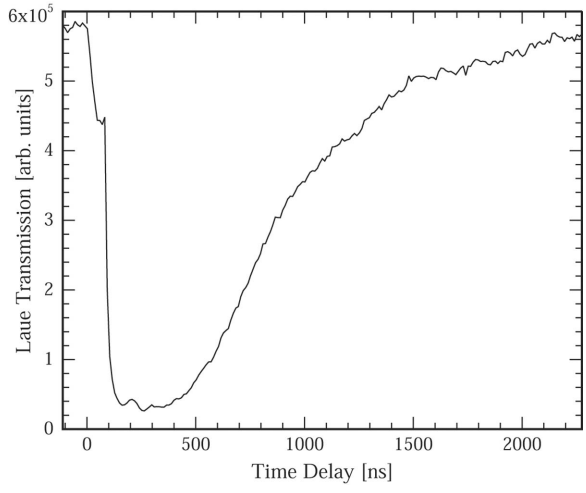

Figure 14
Time-resolved anomalous transmission after intense laser excitation.

Localized static strains or crystal defects can redistribute populations between α and β, changing the relative amplitude of the forward and deflected beams (Authier *et al.*, 1996). If the spatial dimension of the acoustic pulse is much less than a Pendellösung length, this situation can be described as two crystals separated by a very thin strained interface moving at the speed of sound.

We assume that the strained interface acts as a rotation of the $\alpha\beta$ basis by an angle θ (DeCamp, Reis, Bucksbaum, Adams *et al.*, 2001),

$$\begin{bmatrix} \cos\theta & -\sin\theta \\ \sin\theta & \cos\theta \end{bmatrix} \begin{bmatrix} \alpha \\ \beta \end{bmatrix}. \tag{15}$$

After the X-rays interact with the strained region, the transmitted X-ray fields evolve according to dynamical diffraction. Fig. 16 shows the result of this calculation assuming that the acoustic disturbance moves from the output face antiparallel to the X-ray Poynting vector. The amount of rotation is proportional to the strain. Here we use a value of $\pi/40$ rad.

When the acoustic pulse is close to the output face, the X-rays that interact with the strained layer are completely dominated by the α solution since the β solution has long since

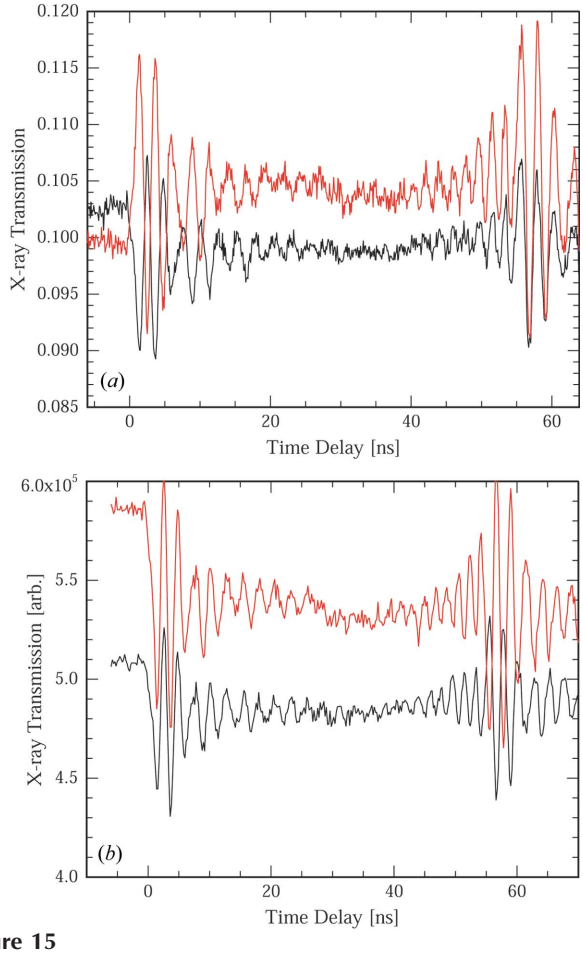

Figure 15
(*a*) X-ray transmission for the 220 symmetric reflection in 001 Ge as a function of time delay. (*b*) Time-resolved diffraction of the symmetric 220 reflection, front side excitation. The upper (lower) curve in each panel corresponds to the deflected (forward) diffracted beam.

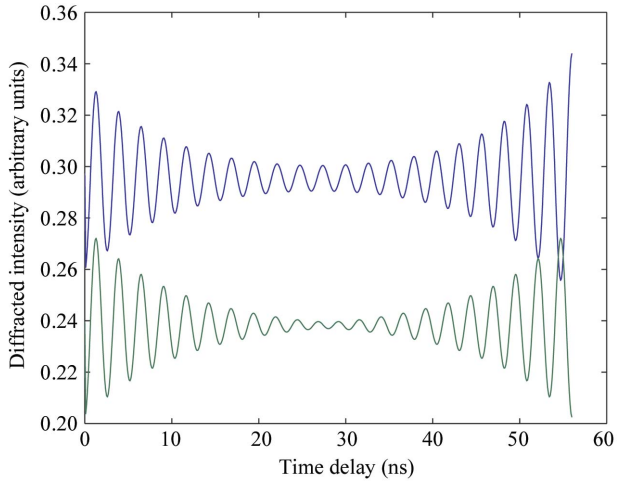

Figure 16
A simulation of the two-crystal model. The upper curve corresponds to the deflected-diffracted beam while the lower curve corresponds to the forward-diffracted beam.

been absorbed. In the presence of the acoustic pulse the β solution can be repopulated. As the acoustic pulse propagates through the crystal, the effective crystal thickness behind the strained region changes over time. The diffracted intensities beat against each other as a function of time (DeCamp, Reis, Bucksbaum, Adams *et al.*, 2001; DeCamp *et al.*, 2003).

If the acoustic disturbance is located closer to the input side, however, both the β and α solutions are populated approximately equally prior to the interaction with the strained layer. The strained layer will simply remix the solutions causing the amount of population in each solution to change as a function of depth. Since there is a large undisturbed crystal following the strained layer, the β solution will be absorbed quickly leaving only the α solution. Since α is the only solution to survive, the beams will be modulated equally.

Although the simple rotation of basis appears to correctly predict the observed modulations, the exact mechanism of the transfer is not immediately obvious since in the symmetric Laue geometry the phonon wavevector ($\mathbf{q}$) is perpendicular to the reciprocal lattice vector. However, in practice, it is very difficult to obtain crystals that are cut perfectly. In this case the crystal was miscut by $\sim$3 mrad allowing the strain to be detectable by the X-ray diffraction. Assuming modest strains, a $\pi/40$ basis rotation is easily attainable.

6.2. Time-resolved asymmetric Laue geometry

The previous two diffraction geometries demonstrated the ability of time-resolved X-ray diffraction to study strain propagation. X-ray diffraction in the Bragg and Laue geometries are complementary. X-ray Bragg diffraction can provide a precise study of strain, but the X-ray probe depth is limited to the X-ray extinction depth (or the X-ray absorption depth). Symmetric X-ray Laue geometry can detect crystalline strain very deep within crystals but, owing to the direction of the reciprocal lattice vector, symmetric Laue geometry is unable to precisely measure a laser-induced strain. Asymmetric Laue geometry can overcome these limitations.

Unlike the symmetric Laue geometry, an asymmetric Laue reflection is one where the reciprocal lattice vector is not perpendicular to the surface normal. Therefore, a laser-generated strain has a component along the reciprocal lattice vector, making the strain easily detectable. The Borrmann effect in the asymmetric Laue geometry is a useful probe for strain pulses propagating through very thick crystals.

In the symmetric geometry, the laser-generated acoustic pulse travels parallel to the surface normal, not the Poynting vector of the diffracting X-rays. To compensate for this potential difficulty, the optical pulse illuminates a relatively large surface area. This provides a large spatial profile to the propagating acoustic pulse and thus the spatial walk off between the acoustic pulse and the X-ray probe is negligible.

For these experiments, a Ge 001 crystal is oriented to diffract from the $20\bar{2}$ diffraction plane. The asymmetry angle is 45° for this reflection, midway between a symmetric Bragg reflection and a symmetric Laue reflection. An ultrafast optical pulse generates an acoustic disturbance on either face of the crystal.

Like the symmetric data, under intense laser excitation the diffraction efficiency of the asymmetric reflection goes to zero for an extended period of time. Unlike the symmetric geometry, as the laser fluence is reduced the diffraction efficiency of the forward beam does not recover. In Fig. 17 the peak diffraction intensity of both the forward and deflected beams of the Ge crystal is shown as a function of time delay. In this case the acoustic pulse was initially generated on the output face of the crystal.

Immediately after the laser absorption (fluence $\sim$5 mJ cm^{-2}), the intensity of the two diffracted beams changes rapidly. The forward beam decreases while the deflected beam increases by the same amount, indicating a coherent transfer of energy. Up to 75% of the X-rays are

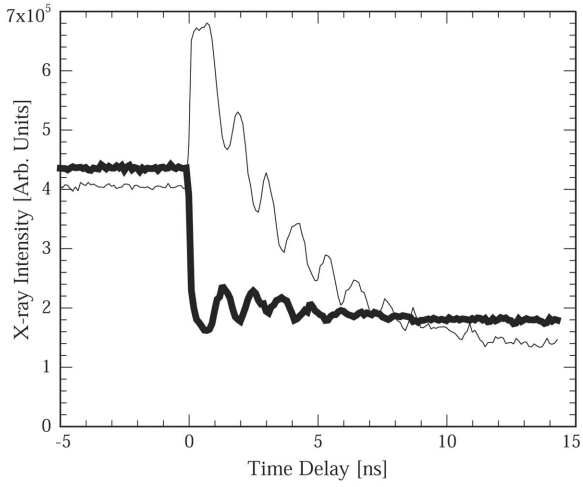

Figure 17
The peak diffraction efficiency of the asymmetric $20\bar{2}$ Laue reflection as a function of laser/X-ray time delay. The thick (thin) line corresponds to the forward (deflected) diffracted beam.

coherently transferred between beams. The time dependence of this phenomenon is comparable with the X-ray pulse width indicating that the switching mechanism is at least as fast as the 100 ps X-ray pulse width.

The population transfer for diffraction from the $\bar{2}02$ diffraction plane (asymmetry -45°) is the mirror image of the $20\bar{2}$ case. The diffracted intensity of the forward beam now decreases while the deflected beam increases. Again, the time scale for transfer appears to be limited by the X-ray pulse width.

The fast phenomenon does not appear to have an angular dependence. This may be due to the wavevector selectivity of the Borrmann effect. In the strained region, like the Bragg case, sidebands on the diffraction peak are generated. The modified Laue condition cannot be satisfied, however, because of the wavevector selectivity of the Borrmann effect. So unlike the Bragg case where sidebands are easily observed, in the Borrmann geometry only those wavevectors which satisfy the Laue condition propagate through the crystal.

Following the rapid population transfer, oscillations in the diffracted intensity are visible. As in the symmetric Laue case, these are Pendellösung oscillations owing to redistribution of the $\alpha\beta$ basis. This is further verified by changing the energy of the incident X-rays. The change in the Pendellösung period is proportional to the crystalline structure factor, which is strongly dependent on the X-ray energy. In Fig. 18 the time-resolved diffraction efficiency is plotted as the incident X-ray energy approaches the Ge K edge (11.10 keV). Although the X-ray energy changes by less than 30 eV (0.3%), the Pendellösung period changes by $\sim$16%. This is due to the imaginary part of the crystal structure factor changing radically as the X-ray energy approaches an absorption edge.

Further changes in the incident optical fluence cause the amplitude of fast X-ray switch and the Pendellösung oscillations to change drastically. Fig. 19 demonstrates the relationship. At relatively low fluences (<8 mJ cm^{-2}) the switch amplitude is proportional to the incident optical intensity. Simultaneously, the relative phase of the Pendellösung oscillation is anti-correlated with the switch amplitude.

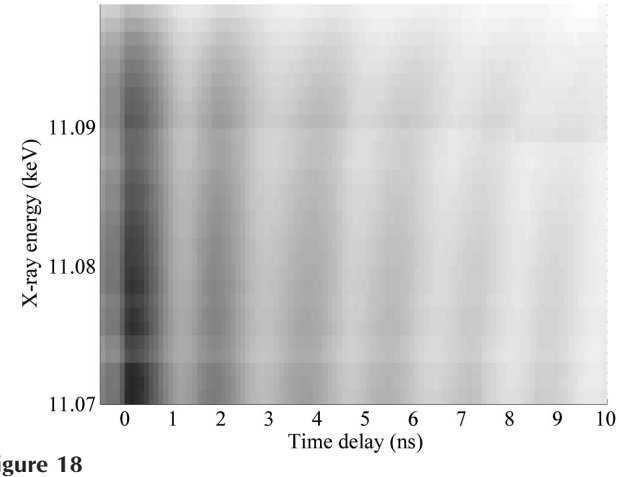

Figure 18
Time-resolved Pendellösung oscillations as the incident photon energy approaches the Ge absorption edge (11.10 keV).

The generation of an acoustic pulse on the input face of the crystal displays similar features. As in the symmetric case, when the acoustic pulse is generated on the input face both diffracted beams initially behave identically. Again this is due to the large unperturbed region beyond the strained crystal layer.

6.3. What is the fast mechanism?

The length scale of diffraction in the thick crystal limit is given by the Pendellösung depth. The fast coherent transfer of energy, however, does not appear to correspond to an acoustic pulse traversing the Pendellösung depth and thus is an unexpected physical phenomenon. To properly diagnose the fast mechanism, an X-ray streak camera is used to detect picosecond changes in the diffracted X-ray intensity. Owing to experimental constraints, the streak camera was only able to sample the forward-diffracted beam. Using the $20\bar{2}$ reflection, the time dependence of the X-ray switch is measured for Ge single crystals.

When the laser pulse arrives, an immediate transfer of energy is apparent in the transmitted beam (Fig. 20). Within 60 ps of illuminating the sample, 75% of the transmitted X-ray intensity is switched. The fall time of this process appears to be $\sim$40 ps which, if we assume that the disturbance moves at the sound speed, represents a depth of $\sim$200 nm or 4% of a Pendellösung depth. Diffracting from the opposite asymmetry, the rising edge of the population transfer can be measured. The rising edge appears to take place in a time consistent with the falling edge.

If the fast switch can be described with dynamical diffraction, the switching mechanism must be related to the Pendellösung depth. For this to occur, the driving mechanism of the fast switch must be one or more of the following; the Pendellösung period changes dynamically with the laser-

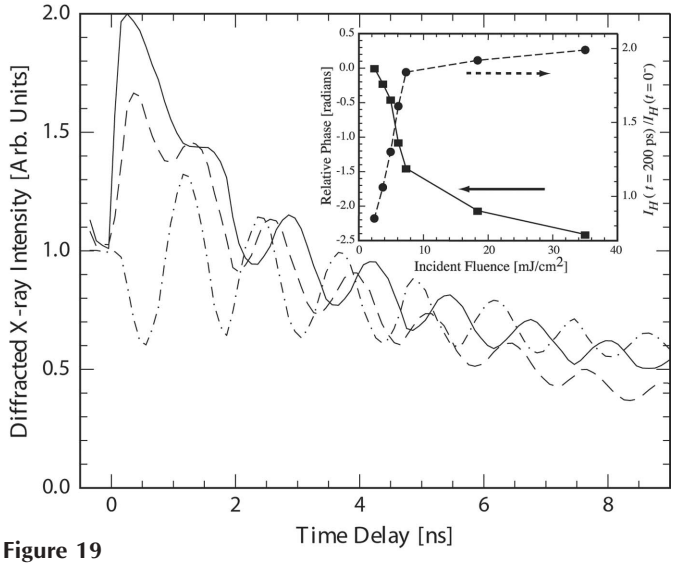

Figure 19
Deflected-diffracted intensity for an incident laser fluence of 35 (solid line), 7 (dashed line) and 2 (dot-dashed line) mJ cm^{-2}. Inset: X-ray switch efficiency and the retrieved phase of the Pendellösung oscillations as a function of optical fluence. Adapted from DeCamp *et al.* (2003).

induced strain, a shockwave is generated, or the strain depth is significantly different from the generally accepted values.

Since the structure factor is related to the density of the material, it is conceivable that the strain could dynamically change the Pendellösung period. However, to generate the necessary change in the Pendellösung period, the strains required are much too large to be a practical consideration. Although a supersonic shockwave appears to be an attractive solution, time-resolved Bragg diffraction does not show any evidence for an acoustic pulse travelling at supersonic velocities. The only remaining plausible explanation is an extended strain depth.

The generation of acoustic strains at depths much larger than the optical penetration depth could be explained by the supersonic expansion of a dense electron–hole plasma. This plasma evolves on the time scale of diffusion, which, if the plasma were dense enough, could explain the fast transfer of X-ray energy. Again it should be noted that, although the electron–hole plasma diffusion is supersonic, the generated acoustic pulse evolves at sonic velocities with an extended spatial profile. The time-resolved Bragg diffraction in Ge appears to support the existence of the electron–hole diffusion generating a very deep strain. However, the limited penetration depth of Bragg diffraction only probes the near-surface region. By utilizing the time-resolved Laue diffraction it is possible to determine the strain-generation mechanism.

Simulating the diffraction patterns by numerically integrating the X-ray wave equations provides the mechanism of the strain generation. If one assumes that the strain generation is determined by the thermo-elastic model with an extended penetration depth ($\sim$1 μm), the fast effect can be modelled; however, the observed phase shift of the Pendellösung oscillations is anti-correlated with the switch amplitude. Using the carrier diffusion model of strain generation, the behavior of switch amplitude and Pendellösung phase shift is correctly predicted (DeCamp *et al.*, 2003).

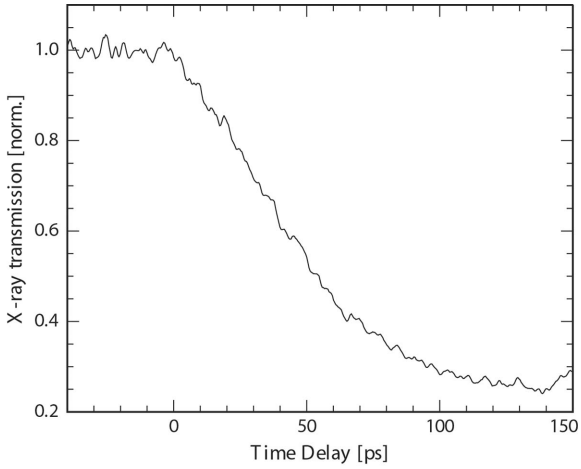

Figure 20
X-ray streak camera data of the transmission efficiency of the asymmetric $20\bar{2}$ reflection in Ge. Adapted from DeCamp *et al.* (2003).

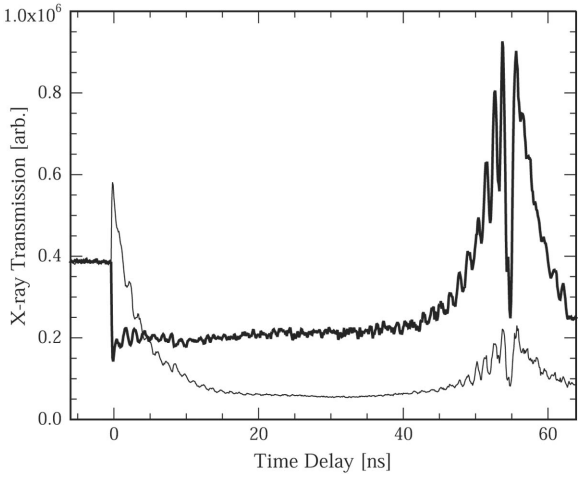

Figure 21
X-ray transmission as a function of acoustic pulse time delay. The acoustic pulse is approaching the input face of the Ge crystal. The thick (thin) line corresponds to the forward (deflected) diffracted beam. Adapted from DeCamp, Reis, Bucksbaum, Adams *et al.* (2001).

6.4. Acoustic reflections

As the acoustic pulse approaches the opposite crystal face of the crystal, a 'Borrmann revival' is observed. As the transmission returns, Pendellösung oscillations in the diffracted intensity are seen. Like the symmetric case, as the acoustic pulse approaches the input face, the oscillations in the two beams are in phase (Fig. 21). As the acoustic pulse collides with the input face of the crystal, the intensity of the forward beam is about 2.5 times that of the static crystal case, *i.e.* greater than the sum of the two diffracted beams of an unstrained crystal.

This dramatic increase in the diffraction efficiency can be explained by the two-crystal model. In the static-crystal case the sum of the output intensities can be no larger than one half of the original input intensity owing to the strong absorption of the β solution. In the ideal situation the intensity increase of one beam owing to the rotation of the $\alpha\beta$ basis on the output face of the crystal is only a factor of two. However, if the basis rotation occurs on the input face, the entire initial β population can be transferred to the α solution, increasing the output of one beam by up to a factor of four. If the acoustic pulse originates from the front side of the crystal, the observed Pendellösung oscillations during the revival are now out of phase and the sum of the two diffracted beams is $\sim$50% that of the unstrained crystal case, consistent with the two-crystal model.

6.5. Acoustic collisions

Although the X-rays diffract through the entire bulk of the crystal, the observational power of the asymmetric Laue reflection is limited by the absorption depth of the β solution. For example, in Ge at an X-ray energy of 10 keV, this limitation prevents the direct observation of the strain pulse at depths deeper than $\sim$25 μm. The repopulation of the β solution deep within the bulk of the crystal can circumvent this problem. In static crystals, buried interfaces or lattice dislocations can repopulate the β solution after many absorption

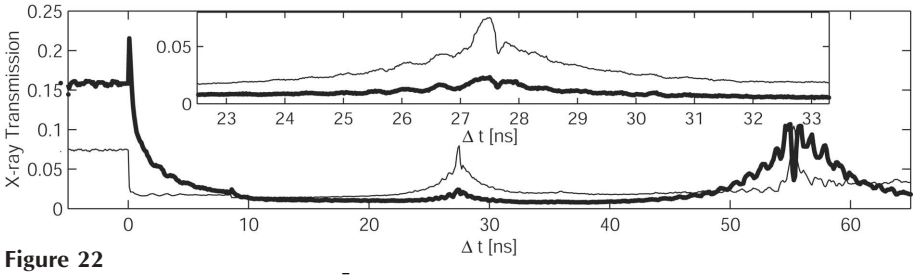

Figure 22
Time-resolved diffraction of the $20\bar{2}$ reflection in Ge. The thick (thin) line corresponds to the deflected (forward) diffracted beam. Inset: the collision time magnified. Adapted from DeCamp, Reis, Bucksbaum, Adams *et al.* (2001).

depths (Authier *et al.*, 1996). Launching a second acoustic pulse, counter-propagating with the first, can produce a transient interface allowing the observation of a transient strain deep within the crystal bulk.

In Fig. 22, two counter-propagating acoustic pulses are generated simultaneously from opposite faces. As expected, immediately after the initial lattice expansion an ultrafast energy transfer has taken place which decays quickly as the acoustic pulses travel into the center of the crystal. At a time delay of ~27.5 ns a Borrmann revival is seen. This time delay corresponds to the acoustic pulses travelling half way through the crystal bulk (DeCamp, Reis, Bucksbaum, Adams *et al.*, 2001).

Like before, the Borrmann revival has oscillations associated with the increase in X-ray transmission; however, in this case the oscillation period is half that of the single acoustic pulse excitation. The reason for the frequency doubling is because, unlike the quasi-two-crystal situation generated by the single acoustic pulse, two acoustic pulses will make a quasi-three-crystal situation. Because the acoustic pulses are counter propagating, the three crystals can be thought of as a single thin crystal contracting (expanding) at twice the speed of sound, sandwiched between two thick crystals expanding (contracting) at the speed of sound. The rapidly changing thin crystal causes the Pendellösung oscillations to oscillate at twice the frequency.

7. Conclusion

The combination of ultrafast lasers and pulsed X-ray beams from third-generation synchrotron facilities has opened up new opportunities for studying the dynamics of materials at picosecond time scales. We have described our results from a dedicated time-resolved diffraction facility at sector 7 of the Advanced Photon Source, Argonne National Laboratory, at which some of the first measurements on transient strain dynamics have been performed. Pump (laser)–probe (X-ray) methods are especially useful for such measurements. The temporal resolution is generally limited by the bunch length (~100 ps) when using gated avalanche photodiode detectors. However, X-ray streak cameras can probe much faster time scales, into the sub-picosecond range. We have demonstrated the coherent control of X-ray beams using impulsively generated phonons, and have shown that this mechanism can be used to slice X-ray pulses. We have also demonstrated a time-resolved version of the Borrmann effect in the asymmetric Laue geometry. We have shown that time-resolved dynamical X-ray diffraction based on this approach is an ideal probe for strain pulses propagating through very thick crystals. Lastly, we used this technique to study the supersonic diffusion of laser-excited electron–hole plasmas in germanium crystals. As these techniques become more refined, studies of complex dynamics in systems such as biomolecules, polymers and liquids should become possible. Recent experiments have begun to use time-resolved X-ray diffraction for the study of protein function (Schotte *et al.*, 2003, 2004) and localized optical phonon oscillations (Sokolowski-Tinten *et al.*, 2003). Ultrafast time-resolved diffraction measurements at today's third-generation X-ray sources will chart the way towards the development of the new linac-based ultrafast X-ray sources which are planned to come on-line at the end of the decade. The Linear Coherent Light Source (LCLS) will produce sub-picosecond X-ray pulses of extreme brightness. A forerunner of LCLS, the Sub-Picosecond Photon Source (SPPS) has just become operational at SLAC/SSRL as an ultrafast X-ray source, offering unprecedented access to the ultrafast hard X-ray regime. These 'fourth-generation' facilities will propel time-resolved X-ray studies into yet new regimes of brightness, short pulse length and coherence to enable many studies that are not possible today. Among these exciting prospects for the future are single-shot measurements on excited state molecular systems and tracking the atomistic motion in structural phase transitions and soft-mode materials such as ferroelectrics.

We thank Adrian Cavalieri, Soo-Heyong Lee and Dohn Arms for experimental assistance. We also thank Roberto Merlin, Justin Wark, Stephen Fahy and our other collaborators. This work was conducted at the MHATT-CAT insertion-device beamline at the Advanced Photon Source and was supported in part by the US Department of Energy, Grants No. DE-FG02-03ER46023 and DE-FG02-00ER15031, and by the NSF Frontiers of Physics Center, FOCUS. Use of the Advanced Photon Source was supported by the US Department of Energy Basic Energy Sciences, Office of Energy Research, under Contract No.W-31-109-Eng-38.

References

Akhmanov, S. A. & Gusev, V. É. (1992). *Sov. Phys. Usp.* **35**, 153–191.
Arms, D., Dufresne, E. M., Clarke, R., Dierker, S. B., Pereira, N. R. & Foster, D. (2002). *Rev. Sci. Instrum.* **73**, 1492–1494.
Authier, A., Lagomarsino, S. & Tanner, B. K. (1996). *X-ray and Neutron Dynamical Diffraction: Theory and Applications.* NATO ASI Series.
Backus, S., Durfee, C. G., Murnane, M. M. & Kapteyn, H. C. (1998). *Rev. Sci. Instrum.* **69**, 1207–1223.
Baron, A. (1997). *Nucl. Instrum. Methods*, A**400**, 124–132.
Bartels, A., Dekorsy, T., Kurz, H. & Kohler, K. (1998). *Appl. Phys. Lett.* **72**, 2844–2846.

Batterman, B. & Cole, H. (1964). *Rev. Mod. Phys.* **36**, 681–716.
Borrmann, G. & Hildebrandt, G. (1956). *Z. Naturforsch Teil A*, **11**, 585–587.
Cavalleri, A., Siders, C. W., Brown, F. L. H., Leitner, D. M., Toth, C., Squier, J. A., Barty, C. P. J., Wilson, K. R., Sokolowski-Tinten, K., von Hoegen, M. H., von der Linde, D. & Kammler, M. (2000). *Phys. Rev. Lett.* **85**, 586–589.
Cavalleri, A., Siders, C. W., Rose-Petruck, C., Jimenez, R., Toth, C., Squier, J. A., Barty, C. P. J., Wilson, K. R., Sokolowski-Tinten, K., von Hoegen, M. H. & von der Linde, D. (2001). *Phys. Rev. B*, **63**, 193306.
Chang, Z., Rundquist, A., Zhou, J., Murnane, M. M., Kapteyn, H. C., Liu, X., Shan, B., Liu, J., Niu, L., Gong, M. & Zhang, X. (1996). *Appl. Phys. Lett.* **69**, 133–135.
Chen, P., Tomov, I. V. & Rentzepis, P. M. (1996). *J. Chem. Phys.* **104**, 10001–10007.
Chin, A. H., Schoenlein, R. W., Glover, T. E., Balling, P., Leemans, W. P. & Shank, C. V. (1999). *Phys. Rev. Lett.* **83**, 336–339.
Cho, G. C., Kutt, W. & Kurz, H. (1990). *Phys. Rev. Lett.* **65**, 764–767.
DeCamp, M. F., Reis, D. A., Bucksbaum, P. H., Adams, B., Caraher, J. M., Clarke, R., Conover, C. W. S., Dufresne, E. M., Merlin, R., Stoica, V. & Wahlstrand, J. K. (2001). *Nature (London)*, **413**, 825–828.
DeCamp, M. F., Reis, D. A., Bucksbaum, P. H. & Merlin, R. (2001). *Phys. Rev. B*, **64**, 092301.
DeCamp, M. F., Reis, D. A., Cavalieri, A., Bucksbaum, P. H., Clarke, R., Merlin, R., Dufresne, E. M., Arms, D. A., Lindenberg, A. M., MacPhee, A. G., Chang, Z., Lings, B., Wark, J. S. & Fahy, S. (2003). *Phys. Rev. Lett.* **91**, 165502.
Dufresne, E. M., Arms, D. A., Clarke, R., Pereira, N. R., Dierker, S. B. & Foster, D. (2001). *Appl. Phys. Lett.* **79**, 4085–4087.
Dufresne, E. M., Arms, D. A., Dierker, S. B., Clarke, R., Yacoby, Y., Pitney, J., MacHarrie, B. & Pindak, R. (2002). *Rev. Sci. Instrum.* **73**, 1511–1513.
Entin, I. R., Suvorov, E. V., Kobelev, N. P. & Soifer, Y. M. (1978). *Fiz. Tverd. Tela*, **20**, 1311–1315.
Garrett, G. A., Albrecht, T. F., Whitaker, J. F. & Merlin, R. (1996). *Phys. Rev. Lett.* **77**, 3661–3664.
Hao, H.-Y. & Maris, H. J. (2000). *Phys. Rev. Lett.* **84**, 5556–5559.
Hao, H.-Y. & Maris, H. J. (2001*a*). *Phys. Rev. B*, **63**, 224301.
Hao, H.-Y. & Maris, H. J. (2001*b*). *Phys. Rev. B*, **64**, 064302.
Hase, M., Mizoguchi, K., Harima, H., Nakashima, S., Tani, M., Sakai, K. & Hangyo, M. (1996). *Appl. Phys. Lett.* **69**, 2474–2476.
Hase, M., Mizoguchi, K., Harima, H., Nakashima, S. & Sakai, K. (1998). *Phys. Rev. B*, **58**, 5448–5452.
Hauer, A. & Burns, S. J. (1975). *Appl. Phys. Lett.* **27**, 524–526.
Helliwell, J. R. & Rentzepis, P. M. (1997). *Time-Resolved Diffraction.* Oxford University Press.
Hunsche, S., Wienecke, K., Dekorsy, T. & Kurz, H. (1995). *Phys. Rev. Lett.* **75**, 1815–1818.
Kishimura, H., Yazaki, A., Kawano, H., Hironaka, Y., Nakamura, K. G. & Kondo, K. (2002). *J. Chem. Phys.* **117**, 10239.
Larson, B. C., White, C. W., Noggle, T. S., Barhorst, J. F. & Mills, D. (1983). *Appl. Phys. Lett.* **42**, 282–284.
Larson, B. C., White, C. W., Noggle, T. S. & Mills, D. (1982). *Phys. Rev. Lett.* **48**, 337–340.
Larsson, J., Chang, Z., Judd, E., Schuck, P. J., Falcone, R. W., Heimann, P. A., Padmore, H. A., Kapteyn, H. C., Bucksbaum, P. H., Murnane, M. M., Lee, R. W., Machacek, A., Wark, J. S., Liu, X. & Shan, B. (1997). *Opt. Lett.* **22**, 1012–1014.
Larsson, J., Heimann, P. A., Lindenberg, A. M., Schuck, P. J., Bucksbaum, P. H., Lee, R. W., Padmore, H. A., Wark, J. S. & Falcone, R. W. (1998). *Appl. Phys. A*, **66**, 587–591.
LeRoux, S. D., Colella, R. & Bray, R. (1975). *Phys. Rev. Lett.* **35**, 230–234.
LeRoux, S. D., Colella, R. & Bray, R. (1976). *Phys. Rev. Lett.* **37**, 1056–1059.
Lide, D. R. (1996). *Handbook of Chemistry and Physics.* Boca Raton, FL: CRC Press.
Lindenberg, A. M., Kang, I., Johnson, S. L., Falcone, R. W., Heimann, P. A., Chang, Z., Lee, R. W. & Wark, J. S. (2002). *Opt. Lett.* **27**, 869–871.
Lindenberg, A. M., Kang, I., Johnson, S. L., Missalla, T., Heimann, P. A., Chang, Z., Larsson, J., Bucksbaum, P. H., Kapteyn, H. C., Padmore, H. A., Lee, R. W., Wark, J. S. & Falcone, R. W. (2000). *Phys. Rev. Lett.* **84**, 111–114.
Liss, K. D., Magerl, A., Hock, R., Remhof, A. & Waibel, B. (1997). *Europhys. Lett.* **40**, 369–374.
Liu, J. Y., Wang, J., Shan, B., Wang, C. & Chang, Z. (2003). *Appl. Phys. Lett.* **82**, 3553–3555.
Merlin, R. (1997). *Solid State Commun.* **102**, 207–220.
Mizoguchi, K., Hase, M., Nakashima, S. & Nakayama, M. (1999). *Phys. Rev. B*, **60**, 8262–8266.
Reis, D. A., DeCamp, M. F., Bucksbaum, P. H., Clarke, R., Dufresne, E., Hertlein, M., Merlin, R., Falcone, R., Kapteyn, H., Murnane, M. M., Larsson, J., Missalla, Th. & Wark, J. S. (2001). *Phys. Rev. Lett.* **86**, 3072–3075.
Rischel, C., Rousse, A., Uschmann, I., Albouy, P. A., Geindre, J. P., Audebert, P., Gauthier, J. C., Förster, E., Martin, J. L. & Antonetti, A. (1997). *Nature (London)*, **390**, 490–492.
Rose-Petruck, C., Jimenez, R., Guo, T., Cavalleri, A., Siders, C. W., Raksi, F., Squier, J. A., Walker, B. C., Wilson, K. R. & Barty, C. P. J. (1999). *Nature (London)*, **398**, 310–312.
Rousse, A., Rischel, C., Fourmaux, S., Uschmann, I., Sebban, S., Grillon, G., Balcou, Ph., Förster, E., Geindre, J. P., Audebert, P., Gauthier, J. C. & Hulin, D. (2001). *Nature (London)*, **410**, 1263.
Rousse, A., Rischel, C. & Gauther, J. (2001). *Rev. Mod. Phys.* **17**, 17–31.
Schoenlein, R. W., Leemans, W. P., Chin, A. H., Volfbeyn, P., Glover, T. E., Balling, P., Zolotorev, M., Kim, K.-J., Chattopadhyay, S. & Shank, C. V. (1996). *Science*, **274**, 236–238.
Schotte, F., Lim, M., Jackson, T. A., Smirnov, A. V., Soman, J., Olson, J. S., Phillips, G. N., Wulff, M. & Anfinrud, P. A. (2003). *Science*, **300**, 1944.
Schotte, F., Soman, J., Olson, J. S., Wulff, M. & Anfinrud, P. A. (2004). *J. Struct. Biol.* **147**, 235–246.
Service, R. F. (2002). *Science*, **298**, 1356–1358.
Siders, C. W., Cavalleri, A., Sokolowski-Tinten, K., Toth, C., Guo, T., Kammler, M., Horn von Hoegen, M., Wilson, K. R., von der Linde D. & Barty, C. P. J. (1999). *Science*, **286**, 1340–1342.
Sokolowski-Tinten, K., Blome, C., Blums, J., Cavalleri, A., Dietrich, C., Tarasevitch, A., Uschmann, I., Förster, E., Kammler, M., Horn-von-Hoegen, M. & Dietrich von der Linde, D. (2003). *Nature (London)*, **422**, 287–289.
Strickland, D. & Mourou, G. (1985). *Opt. Commun.* **56**, 219–221.
Takagi, S. (1962). *Acta Cryst.* **15**, 1311.
Takagi, S. (1969). *J. Phys. Soc. Jpn*, **26**, 1239–1253.
Techert, S., Schotte, F. & Wulff, M. (2001). *Phys. Rev. Lett.* **86**, 2030.
Taupin, D. (1964) *Bull. Soc. Fr. Miner. Crist.* **87**, 469–511.
Thomsen, C., Grahn, H. T., Maris, H. J. & Tauc, J. (1986). *Phys. Rev. B*, **34**, 4129–4138.
Thomsen, C., Strait, J., Vardeny, Z., Maris, H. J., Tauc, J. & Hauser, J. J. (1984). *Phys. Rev. Lett.* **53**, 989–992.
Tischler, J. Z., Larson, B. C. & Mills, D. M. (1988). *Appl. Phys. Lett.* **52**, 1785–1787.
Tomov, I. V., Chen, P. & Rentzepis, P. M. (1998). *J. Appl. Phys.* **83**, 5546–5548.
Uesaka, M., Kotaki, H., Nakajima, K., Harano, H., Kinoshita, K., Watanabe, T., Ueda, T., Yoshii, K., Kando, M., Dewa, H., Kondo, S. & Sakai, F. (2000). *Nucl. Instrum. Methods Phys. Res. A*, **455**, 90–98.
Wark, J. S. (1996). *Contemp. Phys.* **37**, 205–218.
Wark, J. S. & He, H. (1994). *Laser Particle Beams*, **12**, 507–513.
Wark, J. S., Whitlock, R. R., Hauer, A. A., Swain, J. E. & Solone, P. J. (1987). *Phys. Rev. B*, **35**, 9391–9394.

Wark, J. S., Whitlock, R. R., Hauer, A. A., Swain, J. E. & Solone, P. J. (1989). *Phys. Rev. B*, **40**, 5705–5714.
Warren, B. E. (1990). *X-ray Diffraction.* New York: Dover.
Wie, C. R., Tombrello, T. A. & Vreeland, T. Jr (1986). *J. Appl. Phys.* **59**, 3743–3746.
Wiedemann, H. (1993). *Particle Accelerator Physics: Basic Principles and Linear Beam Dynamics.* New York: Springer-Verlag.
Winick, H. (1995). *J. Electron Spectrosc.* **75**, 1–8.
Woolsey, N. C. & Wark, J. S. (1997). *J. Appl. Phys.* **81**, 3023–3037.
Young, J. F. & van Driel, H. M. (1982). *Phys. Rev. B*, **26**, 2147–2158.
Zachariasen, W. H. (1945). *Theory of X-ray Diffraction in Crystals.* New York: John Wiley.
Zeiger, H. J., Vidal, J., Cheng, T. K., Ippen, E. P., Dresselhaus, G. & Dresselhaus, M. S. (1992). *Phys. Rev. B*, **45**, 768–778.
Zolotoyabko, E., Panov, V. & Schvarkov, D. (1993). *Rev. Sci. Instrum.* **64**, 1274–1279.
Zolotoyabko, E., Quintana, J. P., Hoerman, B. H. & Wessels, B. W. (2002). *Appl. Phys. Lett.* **80**, 3159.